AGU PUBLICATIONS

JGR

Journal of Geophysical Research: Oceans

RESEARCH ARTICLE

10.1002/2013JC009419

# Frontogenesis and frontolysis of the subpolar front in the surface mixed layer of the Japan Sea

**Ning Zhao[1], Atsuyoshi Manda[2], and Zhen Han[1,3]**

[1]Key Laboratory of Sustainable Exploitation of Oceanic Fisheries Resources, Ministry of Education, Shanghai Ocean University, Shanghai, China, [2]Graduate School of Fisheries Science and Environmental Studies, Nagasaki University, Nagasaki, Japan, [3]College of Marine Sciences, Shanghai Ocean University, Shanghai, China

**Key Points:**
- The subpolar front (SPF) strengthens from October to December and weakens from January
- Horizontal advection is the dominant factor that strengthens the SPF
- Ekman advection is important for frontogenesis but it plays a secondary role

**Correspondence to:**
Z. Han,
zhhan@shou.edu.cn
N. Zhao,
343599711@qq.com

**Citation:**
Zhao, N., A. Manda, and Z. Han (2014), Frontogenesis and frontolysis of the subpolar front in the surface mixed layer of the Japan Sea, *J. Geophys. Res. Oceans*, *119*, doi:10.1002/2013JC009419.

Received 10 SEP 2013
Accepted 27 JAN 2014
Accepted article online 11 FEB 2014

**Abstract** The frontogenesis and frontolysis processes of the subpolar front (SPF) in the surface mixed layer of the Japan Sea are investigated using state-of-the-art oceanic reanalysis data. The SPF experiences a 9 month weakening period from January to September, which shifts to a strengthening period in October. Our analysis shows that horizontal advection consistently contributes to the intensification of the SPF. After September, as the weakening effect of surface heat flux diminishes, horizontal advection becomes the dominant factor that contributes to changes in the SPF strength. Thus, the SPF enters a 3 month strengthening period. The geostrophic component of horizontal advection provides the most important contribution to strengthening the SPF, acting to intensify the SPF year-round. Ekman advection also promotes SPF strengthening with a smaller but still important contribution. During the weakening period, SPF strength is largely controlled by heat flux. The heat flux, especially the shortwave radiation component, is the primary cause of the surface front disappearance in the summer.

## 1. Introduction

Oceanic frontal zones attract great attention not only in oceanography but also in meteorology. Both observations and numerical experiments have revealed the atmospheric response to sea surface temperature (SST), which is induced by front variability [e.g., *Xie et al*., 2002; *Seo et al*., 2007; *Minobe et al*., 2008]. For example, *Inatsu et al*. [2003] showed that storm tracks are sensitive to the latitude of SST variations. A recent study further discussed an anchoring effect of the SST front on low-level storm tracks and eddy-driven polar front jets [*Ogawa et al*., 2012]. Several regional studies have also shown that the seawater temperature field strongly affects meteorological disturbances [e.g., *Yamamoto and Hirose*, 2007; *Moteki and Manda*, 2013]. The importance of the frontal SST gradient has also been demonstrated in many studies [e.g., *Nonaka et al*., 2009; *Sampe et al*., 2010].

The Japan Sea is a semienclosed marginal sea in the Northwest Pacific (Figure 1) that experiences pronounced seasonal atmospheric and oceanic variations. During winter, the strong winter monsoon brings cold Asian air from the north, resulting in extensive heat loss from the ocean [*Dorman et al*., 2004]. Meanwhile, the Tsushima warm current (TWC), the major Japan Sea inflow, which comes from the Tsushima Strait, exhibits minimal volume transport [*You et al*., 2010]. However, during the summer, a weaker summer monsoon transports air from the south, and a larger volume of water is transported by the TWC [e.g., *Dorman et al*., 2005; *Takikawa and Yoon*, 2005].

Numerous studies have shown that the phenomena that occur in the Japan Sea are very similar to those in the open ocean [e.g., *Chu et al*., 2001; *Gordon et al*., 2002; *Park and Watts*, 2005], including a strong temperature front, which is known as the subpolar front (SPF) [*Park et al*., 2007]. In the Japan Sea, this front is regarded as the primary biogeographical and climatic boundary [*Belkin and Cornillon*, 2003] of two regions: a relatively cold, fresh subpolar region and a warm, saline subtropical region. The spatial structure and temporal evolution of the SPF have been investigated in several regional studies [e.g., *Chu et al*., 2001; *Isoda et al*., 1991; *Park et al*., 2004, 2007]. However, only a few of these studies analyzed SPF variability mechanisms. *Isoda* [1994] suggested that seasonal SST variations in the Japan Sea are closely related to the formation of the mixed layer and that the SPF disappears as a result of surface water warming. *Choi et al*. [2009] performed several numerical simulations to simulate the variability of SPF on seasonal and interannual

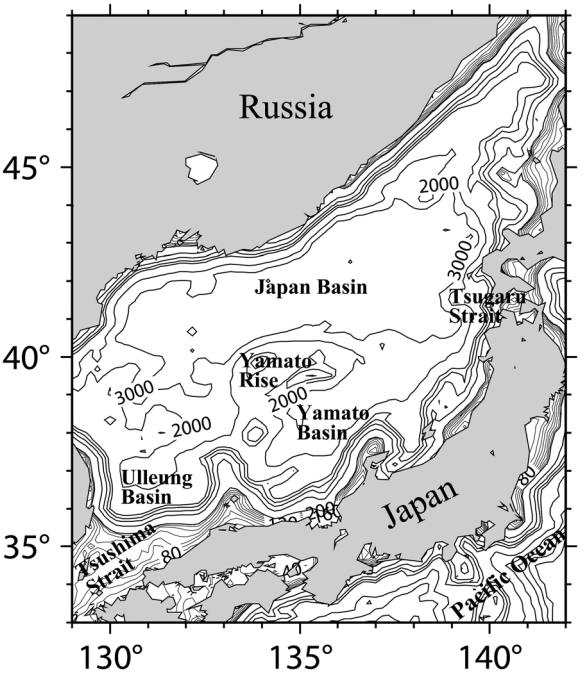


**Figure 1.** Topographic features and bathymetry (in m) of the Japan Sea.

timescales. They found that the SPF was strongly affected by wind stress on these scales. However, a detailed quantitative analysis of the SPF remained unaddressed in these studies.

The goal of this study is to evaluate the seasonal variation of the SPF and to determine the term in the thermodynamic equation that primarily causes SPF frontogenesis and frontolysis in the Japan Sea. The methods and data are described in section 2. The temporal evolution of the SPF is analyzed and discussed in section 3. Section 4 provides a summary of the conclusions.

## 2. Materials and Methods

### 2.1. Data

Water temperature, salinity, velocity, and sea surface height data produced by the Japan Coastal Ocean Predictability Experiment 2 (JCOPE2) ocean reanalysis system are used in this study. Readers are referred to *Miyazawa et al.* [2009] for specific details regarding the JCOPE2 system. In addition to temperature, salinity, and horizontal velocity fields, the JCOPE2 provides two types of surface flux data: shortwave radiation (SW) and the sum of longwave radiation, sensible and latent heat fluxes (WTSURF). The horizontal and temporal resolutions of the JCOPE2 data set are 1/12° × 1/12° and 1 day, respectively. All data are interpolated to a 1° × 1° grid and averaged over 1 week, as described by *Qiu and Kawamura* [2012]. The interpolated and weekly averaged data are used for the mixed layer model described below; the model results are averaged to climatological monthly mean values.

### 2.2. Mixed Layer Model

Previous studies have suggested several methods for defining the mixed layer [e.g., *Kara et al.*, 2003; *Levitus*, 1983; *Thomson and Fine*, 2003]. In this study, the mixed layer is defined according to a density-based criterion ($\sigma_{mld}=\sigma_{ref}+\Delta\sigma_t$, where $\sigma$ is calculated using $\sigma=\rho$-1000). The density difference between the reference depth and the base of the mixed layer is given by

$$\Delta\sigma_t=|\sigma(T_{ref}+\Delta T, S_{ref}, P)\text{-}\sigma(T_{ref}, S_{ref}, P)|, \tag{1}$$

where $T_{ref}$ is the sea water temperature at the reference depth, which is set to 10 m in this study; $\rho$ is the water density; $\Delta T$ is the temperature threshold, which is set to 0.5 K; $S_{ref}$ is the salinity at the reference depth; and $P$ is the water pressure at the sea surface, which is set to 0.

By vertically integrating the energy conservation equation from the base of the mixed layer to the sea surface, the heat budget for the mixed layer can be written as

$$\frac{\partial T}{\partial t}=\frac{Q_{NET}-Q(-h)}{\rho_0 c_p h}-\mathbf{U}\cdot\nabla T-\nabla\cdot\mathbf{U}'T'-\frac{w\Delta T}{h}+res, \tag{2}$$

where $h$ and $T$ represent the MLD and MLT, respectively [*Moisan and Niiler*, 1998]. The left-hand side is the MLT tendency (rate of time change). The first term on the right-hand side is the heat flux term; $\rho_0$ is the reference seawater density (i.e., 1025 kg m$^{-3}$) and $Q_{NET}$ is the net surface heat flux at the sea surface, including

both the shortwave radiation and the sum of the long wave radiation, latent heat flux, and sensible heat flux. Positive heat fluxes indicate that the ocean gains heat. Moreover, $c_p$ is the specific heat of seawater at constant pressure (i.e., 3986 J kg$^{-1}$ K$^{-1}$). The penetrative radiative flux at the base of the mixed layer, $Q(-h)$, is given by

$$Q(-h)=Q(0)[R\exp(-h/\gamma_1)+(1\text{-}R)\exp(-h/\gamma_2)], \tag{3}$$

where $Q(0)$ is the shortwave radiation at the sea surface and $R$, $\gamma_1$, and $\gamma_2$ are 0.58, 0.35, and 23, respectively, which correspond to type I water [*Paulson and Simpson*, 1977]. The second term on the right-hand side of equation (2), $\mathbf{U}\cdot\nabla T$, represents the horizontal advection due to the climatological monthly mean current and temperature, where $\mathbf{U}$ is the horizontal velocity vector averaged vertically from the sea surface to the base of the mixed layer. The third term, $\nabla\cdot\mathbf{U}'T'$, is the horizontal eddy term, which is the covariance between the temperature and horizontal velocity anomalies from the climatological monthly means. The fourth term, $w\Delta T/h$, is the entrainment term. The entrainment velocity, $w$, is given by

$$w=\frac{\partial h}{\partial t}+\mathbf{u}_{-\mathrm{h}}\cdot\nabla h+w_{-h}, \tag{4}$$

where $\mathbf{u}_{-\mathrm{h}}$ and $w_{-h}$ are the horizontal and vertical velocities at the base of the mixed layer, respectively. In this study, the entrainment velocity is set to 0 during the detraining period. Moreover, $\Delta T$ is the temperature difference between the mixed layer and the layer just below the mixed layer. The last term on the right-hand side of equation (2), *res*, represents the residual term, which includes such processes as horizontal diffusion and vertical shear term; these residual processes are not represented in this study. Readers are referred to *Stevenson and Niiler* [1983] and *Moisan and Niiler* [1998] for details on the mixed layer model.

### 2.3. Temperature Gradient and its Evolution

Because the meridional gradient in the climatological MLT is much larger than the longitudinal gradient in the SPF region of the Japan Sea, the gradient magnitude (GM), which was introduced by *Kazmin and Rienecker* [1996], is employed to measure the SPF intensity of

$$GM=-\frac{\partial T}{\partial y}, \tag{5}$$

where $y$ is the meridional coordinate. The diagnostic equation that describes the temporal evolution of the GM can be obtained by taking the derivative of equation (2) with respect to $y$

$$\frac{\partial GM}{\partial t}=-\frac{\partial}{\partial y}\left(\frac{Q_{NET}-Q(-h)}{\rho_0 c_p h}\right)+\frac{\partial}{\partial y}(\mathbf{U}\cdot\nabla T)+\frac{\partial}{\partial y}(\nabla\cdot\mathbf{U}'T')+\frac{\partial}{\partial y}\left(\frac{w\Delta T}{h}\right)-\frac{\partial}{\partial y}(res). \tag{6}$$

Figure 2 shows the GM and MLT horizontal distributions in the Japan Sea. Most of the SPF is located in the region defined by 37.5–41.5°N, 130.5–137.5°E (henceforth called the SPF region), which is represented by a black box in the figures (e.g., Figure 2). The SPF has a pronounced seasonal variation, strengthening from November to June and becoming very weak from July to October. The strongest SPF appears in December and January with a GM greater than 2 K (100 km)$^{-1}$ in the central SPF region.

### 2.4. Data Validation

Although the JCOPE2 reanalysis system assimilates in situ and satellite-based data, we still provide a comparison of the JCOPE2-derived SSTs with the satellite-derived synthesis data to ensure the credibility of our results. In this section, the NOAA Optimum Interpolation Sea Surface Temperature V2 data (OISST) [*Reynolds et al*., 2002] are used for data validation. Following algorithm defined above, the weekly 1° × 1° OISSTs and JCOPE2 SSTs are first obtained. Then, the differences between the JCOPE2 SSTs and OISSTs are calculated and are subsequently averaged to a climatological monthly mean. As shown in Figure 3, the differences are relatively small throughout the year.

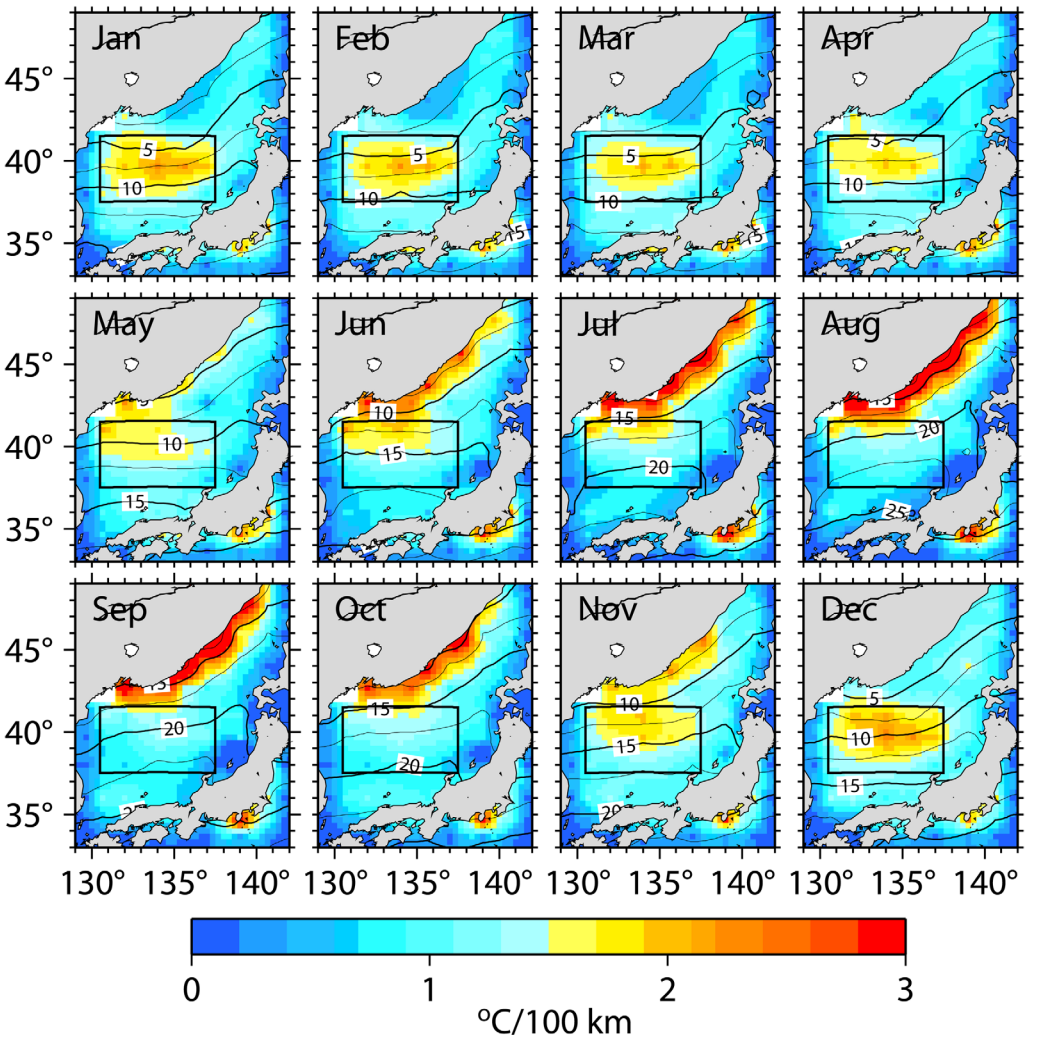


**Figure 2.** GM (color shaded) and MLT isotherms (every 2.5°C) in the Japan Sea. The black boxes represent the SPF region.

## 3. Results

### 3.1. Mixed Layer Temperature

The temporal evolutions of the MLD and the MLT (averaged within the SPF region) are shown in Figure 4. In the SPF region, the MLT increases during spring and summer and decreases in autumn and winter. However, the MLD is more stable in most months until the onset of the winter monsoon.

Figure 5 shows the horizontal distribution of the MLT tendency term in equation (2). During May and June in the SPF region, the tendency term in the northern area is larger than that in the southern area. Similarly, the largest cooling tendency also originates at the northernmost boundary of the SPF region in October. Furthermore, the cooling effect expands to the entire northern SPF region by late November and exceeds $-1.5 \times 10^{-6}$ K s$^{-1}$. This tendency distribution leads to strong temperature gradients, which will be shown later.

### 3.2. Temporal Evolution of the SPF

The variation in the GM tendency shows that the SPF weakening period is longer than the strengthening period (Figure 6). From January to September, the SPF weakens with an average rate of approximately $-0.4 \times 10^{-7}$ K s$^{-1}$ (100 km)$^{-1}$. In October, the SPF begins to rapidly strengthen. In the northwest SPF region, the GM tendency becomes very high and exceeds $1.3 \times 10^{-7}$ K (100 km)$^{-1}$ s$^{-1}$, which expands to nearly the entire

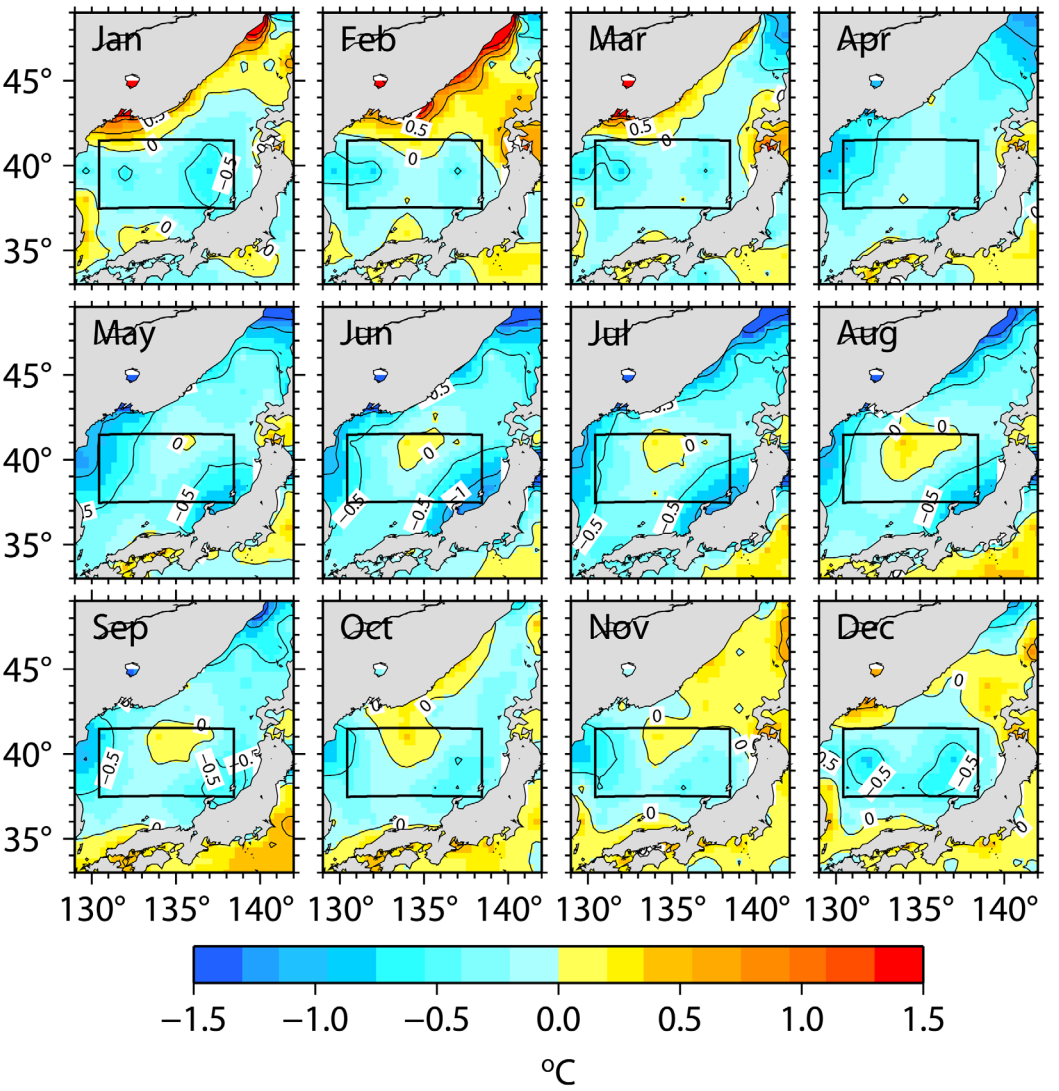


**Figure 3.** The differences between the JCOPE2 SSTs and OISSTs (K).

SPF region in November. The strengthening magnitude decreases in December and ultimately becomes negative again in January.

Area averages of the terms in equation (6) within the SPF region are shown in Figure 7a. The analysis here shows that horizontal advection plays the most important role in maintaining the SPF intensity. Moreover, the heat flux dominates the weakening of the GM. Entrainment weakens the SPF (Figure 7a) from November to May; however, the maximum entrainment contribution is only $-0.3 \times 10^{-7}$ K (100 km)$^{-1}$ s$^{-1}$. The smallest term in equation (6) is the horizontal eddy term, with a contribution of approximately $-0.2 \times 10^{-8}$ K (100 km)$^{-1}$ s$^{-1}$.

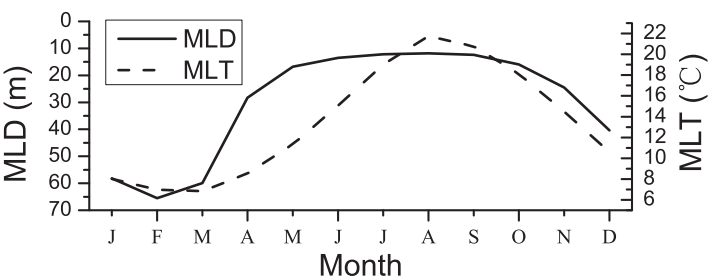


**Figure 4.** Seasonal variations in the area-averaged MLT and MLD in the central region of the Japan Sea (37–42°N, 130–140°E).

In October, horizontal advection weakens. Meanwhile,

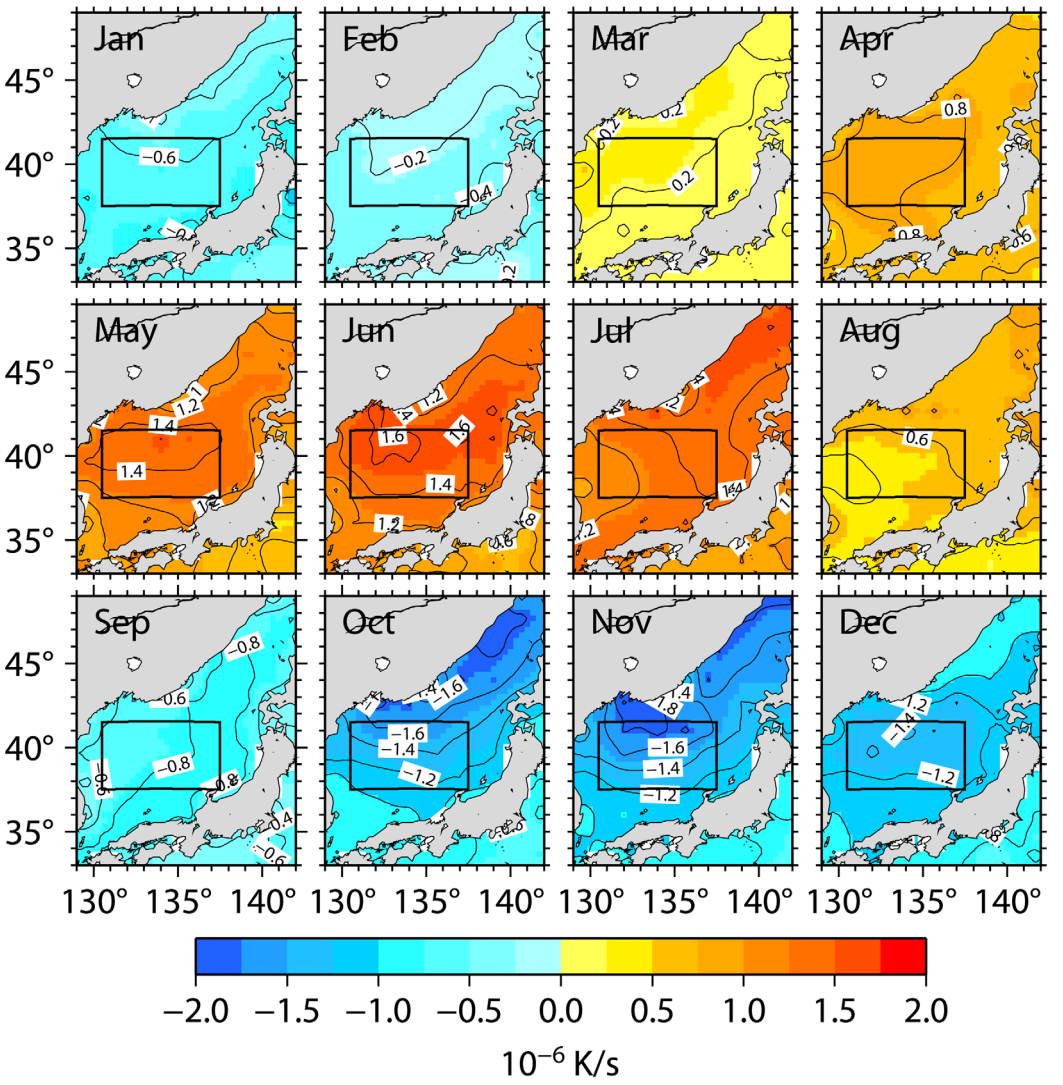


**Figure 5.** MLT tendency in the Japan Sea.

the surface flux term becomes positive, indicating that both the horizontal advection and surface heat flux intensify the SPF, which is different from the SPF weakening period. Consequently, the SPF enters a strengthening period (Figure 7a). When the horizontal advection term reaches its minimum in December, the SPF strengthening period ends. Although the contribution of horizontal advection increases again in January, it does offset the weakening effects until the following autumn. The effect of horizontal advection is discussed in more detail in section 3.3.

During the 9 month weakening period, heat flux provides the largest contribution to the MLT variation. The heat flux weakens the SPF nearly all year, especially from late spring to summer (Figure 7a), reaching a maximum in May with a value of $-2.1 \times 10^{-7}$ K (100 km)$^{-1}$ s$^{-1}$. Compared to the effect of heat flux, all other terms in equation (6) are small. This situation ends in October because the heat flux contribution suddenly decreases to approximately $-0.3 \times 10^{-7}$ K (100 km)$^{-1}$ s$^{-1}$.

To determine the cause of the decrease in the heat flux contribution, the heat flux is separated into three components: shortwave radiation, WTSURF, and penetrative radiative flux (Figure 7b). From January to March, shortwave radiation does not exhibit any pronounced effects on the SPF. Instead, the WTSURF dominates the SPF weakening effect. However, the weakening effect is relatively small during this period; therefore, the SPF remains strong.

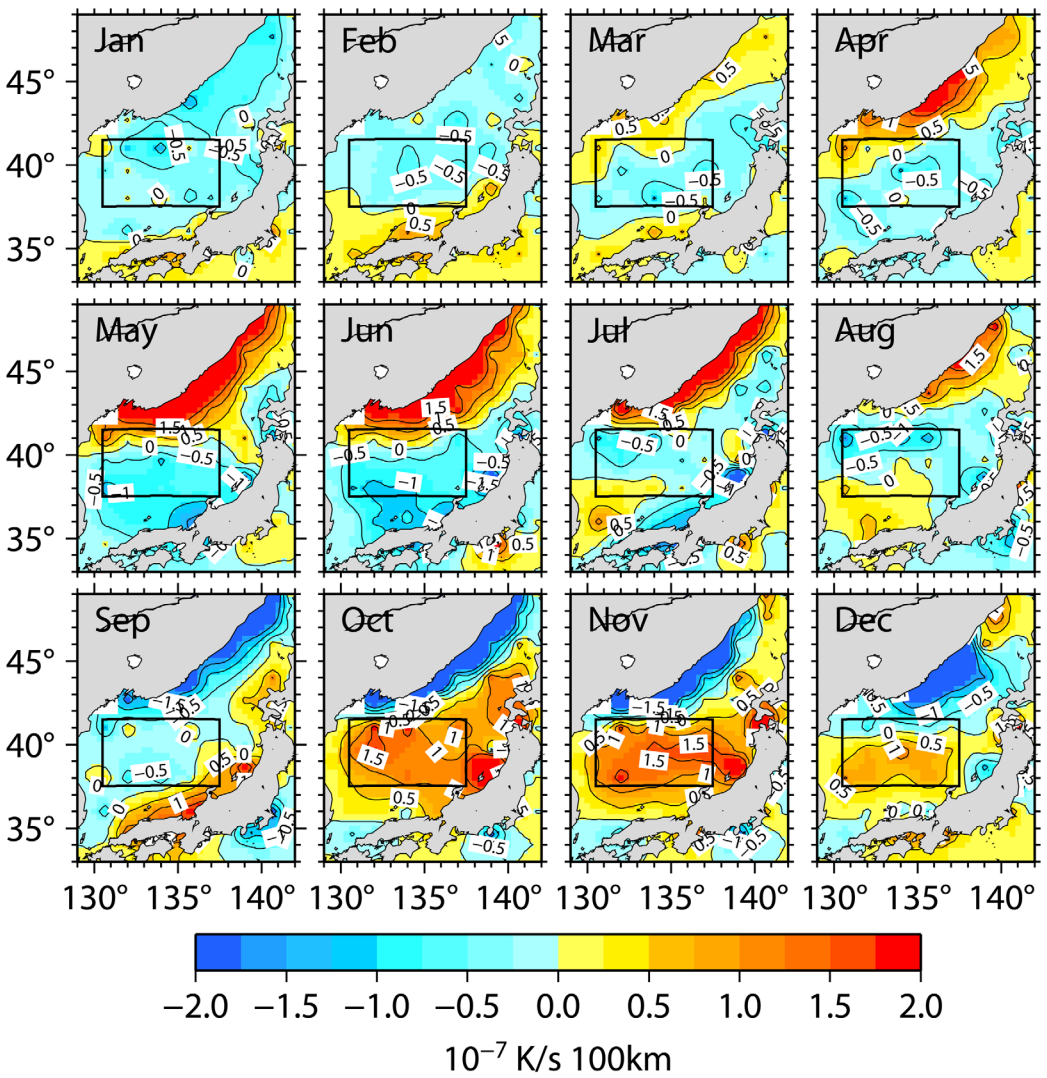


**Figure 6.** GM tendency in the Japan Sea.

After April, strong shortwave radiation ($>$200 W m$^{-2}$) causes strong surface heating (Figure 8). This heating effect is quite uniform, and the temperature increases rapidly in the entire Japan Sea. In the northern region, the shallower MLD promotes a more rapid increase in the MLT than in the southern region and the largest difference is $>0.8 \times 10^{-6}$ K s$^{-1}$. The sharpness of the temperature front at the surface is largely reduced. As shown in Figure 8, the SPF wakens by $>-0.2 \times 10^{-6}$ K s$^{-1}$ (100 km)$^{-1}$ due to the shortwave radiation weakening effect during this period. Moreover, shortwave radiation decreases rapidly (Figure 7b) and ultimately causes the disappearance of the SPF in the surface mixed layer in summer.

High shortwave radiation and a shallow mixed layer also allow more heat to penetrate into deeper layers of the water column. As a result, the penetrative radiative heat flux increases (Figure 7b). However, in comparison with other fluxes, the increase is too small to offset the weakening effects of shortwave radiation and WTSURF.

Unlike shortwave radiation, the weakening effect of WTSURF has a steadier tendency during most times of the year. However, the WTSURF acts to strengthen the SPF in the late autumn. This change balances the shortwave radiation weakening effect and causes a decrease in the total heat flux contribution.

The MLT used in this study might reflect a substantial effect of data assimilation because the residual term becomes large relative to the other terms in December (Figure 7a). The effect of SST corrections may be

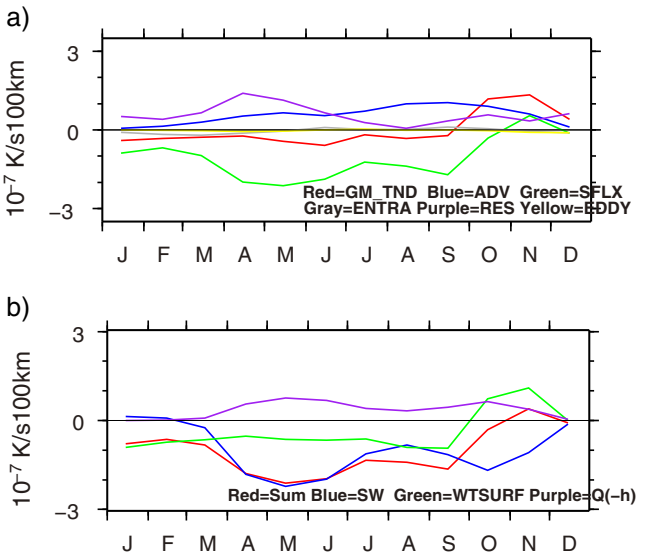


**Figure 7.** (a) Time series of the terms (averaged over the SPF region) in equation (6). (b) Contributions of the heat flux components (averaged over the SPF region), including the surface heat fluxes (i.e., SW and WTSURF) and penetrative radiative flux at the base of the mixed layer, $Q(-h)$.

included in the residual terms in equations (3) and (6), which primarily be attributed to local air-sea heat fluxes. Therefore, the surface heat flux effect might be stronger than the horizontal advection term in December. However, the main mechanism for frontogenesis in fall and winter is the change in the dominant term in the energy balance between the weakening and the strengthening periods. Specifically, during the weakening period, the heat flux cancels the horizontal advection; however, during the strengthening period, both the heat flux and horizontal advection intensify the SPF. The residual term intensifies the SPF throughout the year; however, the magnitude of the residual term is smaller than the surface heat flux during the weakening period. If the entire residual term contributes to the surface heat flux, the sum of the surface heat flux and the residual terms would decrease the GM during the weakening period. Thus, it is unlikely that the residual would contradict the primary mechanism discussed here. The residual term also becomes large relative to the other terms in equation (6) in April, which may be attributed to the imperfect turbulence closure scheme used in the JCOPE2 system during the shoaling phase of the surface mixed layer [e.g., *Noh and Kim*, 1999]. However, the sum of the surface heat flux and the residual term is negative, which indicates that even though the entire residual is due to the surface heat flux, the conclusion that the surface heat flux contributes to the frontolysis of the SPF is not violated.

### 3.3. Effects of Horizontal Advection

To further analyze the contribution of horizontal advection during the strengthening period, geostrophic advection, and horizontal Ekman advection (hereafter Ekman advection) are estimated in the SPF region (Figures 9 and 10). The wind data are obtained from the National Centers for Environmental Prediction/National Center for Atmospheric Research (NCEP/NCAR) reanalysis I data set; the sea surface height (SSH) data are obtained from the JCOPE2 data set. In the mixed layer, the vertically averaged Ekman velocity can be calculated using

$$\mathbf{U}_e = \frac{\tau}{\rho_0 f h} \times \mathbf{k}, \tag{7}$$

where $\tau$ is the wind stress vector, $f$ is the Coriolis parameter, and $\mathbf{k}$ is the vertical unit vector. The geostrophic velocity in the mixed layer can be obtained using

$$\mathbf{U}_g = \frac{g}{f}\mathbf{k} \times \nabla \eta, \tag{8}$$

where $\eta$ is the sea surface height and $g$ is the acceleration due to gravity (i.e., 9.8 m $s^{-2}$). The sea surface height fields are smoothed in time (weekly) and space ($1^\circ \times 1^\circ$) to avoid unexpected short-term fluctuations before computing the geostrophic velocity.

Beginning in January, horizontal advection slowly increases and reaches a maximum in September. Our analysis demonstrates that geostrophic advection contributes more than Ekman advection to the total

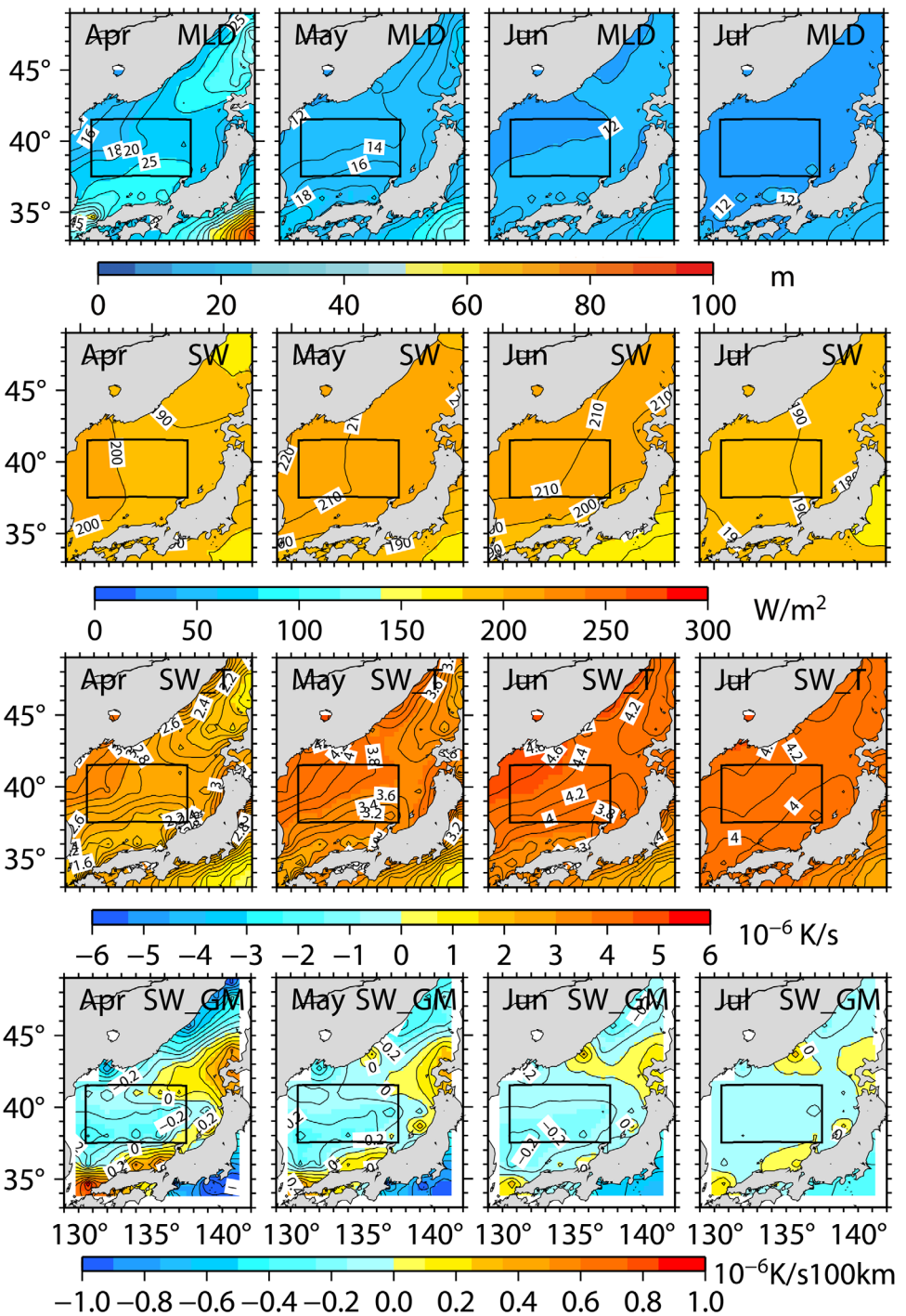


**Figure 8.** Spatial distributions of the mixed layer depth (MLD), the shortwave radiation flux (SW, downward positive), the MLT tendency due to shortwave radiation (SW_T) and the contribution of the shortwave radiation term in equation (6) (SW_GM).

horizontal advection, accounting for >70% of the horizontal advection term (Figure 9). Ekman advection is generally small. However, Ekman advection provides some important contributions in September and October.

Geostrophic advection strengthens the SPF throughout the year (Figure 9). Beginning in spring, geostrophic advection slowly increases, which is followed by a more rapid increase in summer, preceding the maximum horizontal advection in September. Although geostrophic advection gradually decreases over the following

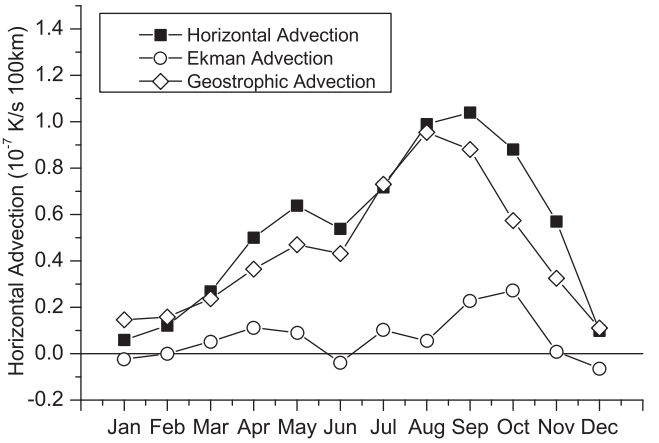


**Figure 9.** Area-averaged contributions of horizontal advection, geostrophic advection, and Ekman advection in the SPF region.

4 months (Figure 10), the strengthening effect remains strong ($0.1 \times 10^{-6}$ K $s^{-1}$ (100 km)$^{-1}$) in the central SPF region. According to previous studies, the main geostrophic current is the branch of the Tsushima current in the SPF region (38–40°N). The horizontal maps of $\eta$ and MLT indicate strong northward geostrophic advection across the southern extent of the SPF region and eastward geostrophic advection near the northern extent of the SPF region, which indicate the convergence of the horizontal heat flux in the SPF region (not shown). The current velocity increases from July to September and decreases in winter [*Chu et al*., 2001]. We believe that the current plays an important role in the increasing advection contribution that promotes the strengthening of the SPF.

The contribution of Ekman advection is much smaller than for geostrophic advection throughout most of the year. Regardless, Ekman advection is important for the SPF. As shown in Figure 9, Ekman advection accounts for >30% of the horizontal advection in October, which is when the Japan Sea begins transitioning to winter conditions [*Chu et al*., 2005]. In the central part of the SPF region, Ekman advection tendency is $0.6 \times 10^{-7}$ K (100 km)$^{-1}$ $s^{-1}$. Later, as the winter monsoon strengthens, Ekman advection decreases. The horizontal map also shows that Ekman advection decreases rapidly in the northern SPF region (Figure 10). However, in the south SPF region, Ekman advection continually strengthens the SPF with a relatively small but persistent contribution.

## 4. Summary

In this study, the frontogenesis and frontolysis processes of the subpolar front (SPF) in the surface mixed layer of the Japan Sea are investigated using oceanic reanalysis data. In the Japan Sea, the MLT increases from March to August and decreases throughout the rest of the year. Compared with the southern SPF region (Figure 4), the northern SPF region exhibits larger temperature variations. Unlike the MLT, the SPF itself experiences a 9 month weakening period that begins in January and shifts to a strengthening period in October; the strongest SPF appears in December. The maximum strengthening of the SPF is $>1.3 \times 10^{-7}$ K (100 km)$^{-1}$ $s^{-1}$, while the weakening averages only $-0.4 \times 10^{-7}$ K (100 km)$^{-1}$ $s^{-1}$.

The analysis in this study indicates that horizontal advection is the main factor that strengthens the SPF. Horizontal advection provides consistent year-round positive contributions to the SPF that slowly increase in January and reach a maximum reaching its peak value in September. In October, as the weakening effect on the SPF subsides, horizontal advection begins to dominate the SPF. Although horizontal advection decreases after October, it continues to be the predominant factor until the following January. Thereafter, the SPF experiences a 3 month strengthening period.

Using sea surface height and wind data, the contributions of Ekman advection and geostrophic advection are evaluated. Geostrophic advection provides the largest contribution to the total horizontal advection. Although geostrophic advection gradually decreases after September, its strengthening effect remains strong in the central SPF region. Ekman advection exhibits its largest contribution to the SPF in October. Afterward, as the winter monsoon becomes stronger, the contribution of Ekman advection decreases and promotes a weakening of the SPF in the northern region. However, Ekman advection continually strengthens the SPF in the southern region.

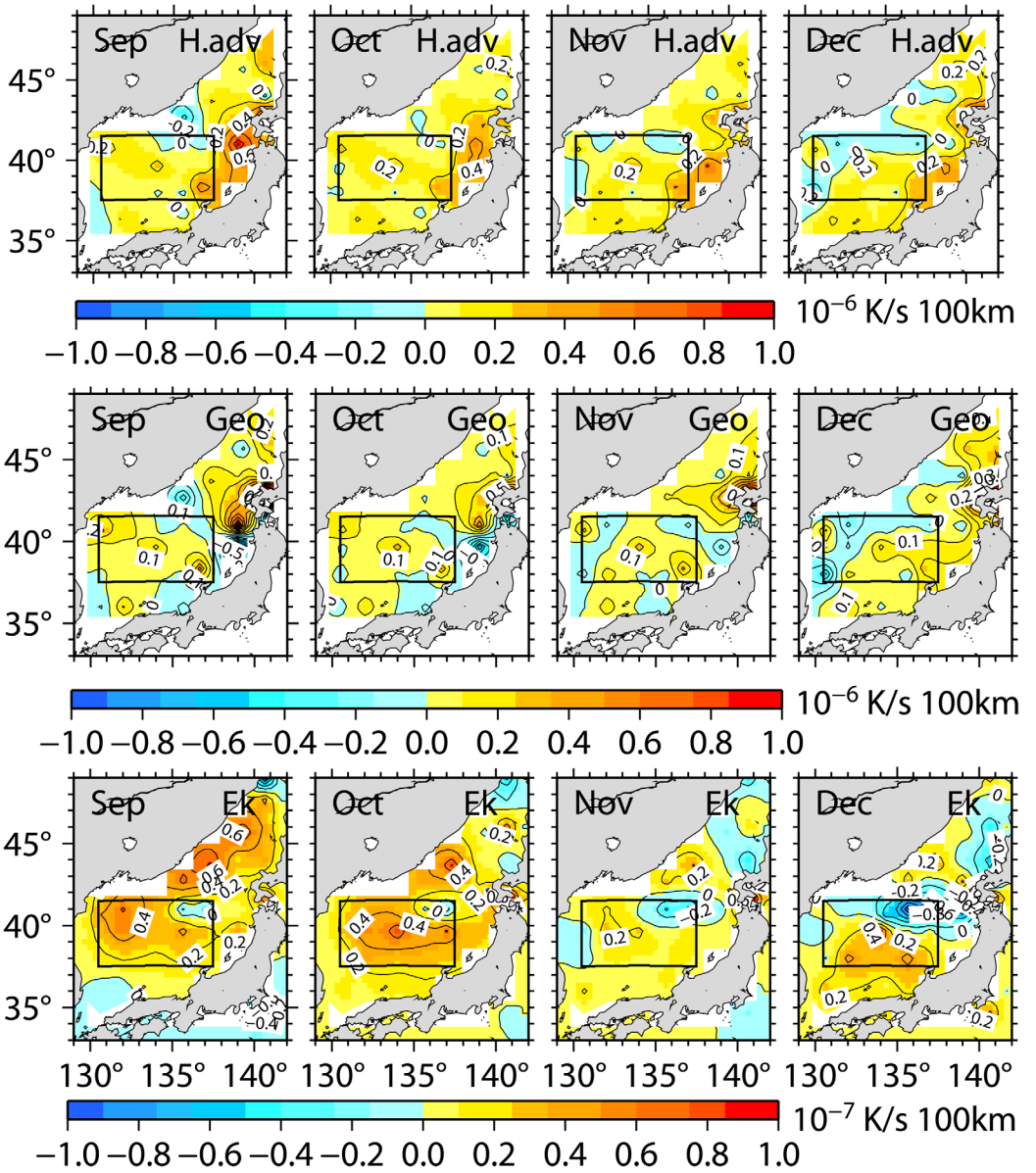


**Figure 10.** Spatial distributions of horizontal advection (H.adv), geostrophic advection (Geo), and Ekman advection (Ek) from equation (6). Note that the scale of Ekman advection is different from the other terms.

Furthermore, the heat fluxes contribute the largest weakening effect on the GM. When the heat flux is decomposed into its components, the shortwave radiation component is found to dominate the other components during the weakening period. Shortwave radiation also provides strong surface heating during summer, which is the primary cause for the disappearance of the SPF in the surface mixed layer. Further analysis shows that the WTSURF also promotes the strengthening of the SPF in October.

Although the analysis in this study provides insights on the mechanisms that determine the seasonal migration of the SPF, variations on other scales (such as interannual variations) are not included in this study. Many studies have shown that the TWC experiences interannual variations [e.g., *Hirose and Fukudome*, 2006; *Hirose et al*., 2009]; however, its effects on the SPF remain unclear. Detailed analysis of the interannual variations in the SPF and the TWC effects on the SPF should be a topic of future research endeavors.

**Acknowledgments**
The authors would like to thank Y. Miyazawa and R. Zhang for providing the JCOPE2 reanalysis data. We also thank the editor of Journal Geophysical Research-Oceans and two reviewers for their insightful comments. This work was supported in part by the Japan Society for Promotion for Science (JSPS) through a Grant-in-Aid for Scientific Research 22244057 and also by the Japanese Ministry of Education, Culture, Sports, Science, and Technology (MEXT) through a Grant-in-Aid for Scientific Research 22106003 on Innovative Areas 2205. N. Zhao and Z. Han are also supported by the Foundation of Key Laboratory of Integrated Monitoring and Applied Technology for Marine Harmful Algal Blooms (MATHAB) 201401.

## References

Belkin, I., and P. Cornillon (2003), SST fronts of the Pacific coastal and marginal seas, *Pac. Oceanogr.*, *1*(2), 90–113.
Choi, B. J., D. B. Haidvogel, and Y. K. Cho (2009), Interannual variation of the polar front in the Japan/East Sea from summertime hydrography and sea level data, *J. Mar. Syst.*, *78*(3), 351–362, doi:10.1016/j.jmarsys.2008.11.021.
Chu, P. C., J. Lan, and C. Fan (2001), Japan Sea thermohaline structure and circulation. Part I: Climatology, *J. Phys. Oceanogr.*, *31*(1), 244–271, doi:10.1175/1520-0485(2001)031<0244:JSTSAC>2.0.CO;2.
Chu, P. C., C. L. Fang, and C. S. Kim (2005), Japan/East Sea model predictability, *Cont. Shelf Res.*, *25*(17), 2107–2121, doi:10.1016/j.csr.2005.03.006.
Dorman, C., R. Beardsley, R. Limeburner, S. Varlamov, M. Caruso, and N. Dashko (2005), Summer atmospheric conditions over the Japan/East Sea, *Deep Sea Res., Part II*, *52*(11), 1393–1420, doi:10.1016/j.dsr2.2004.09.033.
Dorman, C. E., R. C. Beardsley, N. Dashko, C. Friehe, D. Kheilf, K. Cho, R. Limeburner, and S. Varlamov (2004), Winter marine atmospheric conditions over the Japan Sea, *J. Geophys. Res.*, *109*, C12011, doi:10.1029/2001JC001197.
Gordon, A. L., C. F. Giulivi, C. M. Lee, H. H. Furey, A. Bower, and L. Talley (2002), Japan/East Sea intrathermocline eddies, *J. Phys. Oceanogr.*, *32*(6), 1960–1974, doi:10.1175/1520-0485(2002)032<1960:JESIE>2.0.CO;2.
Hirose, N., and K. I. Fukudome (2006), Monitoring the Tsushima Warm Current improves seasonal prediction of the regional snowfall, *SOLA*, *2*, 61–63, doi:10.2151/sola.2006-016.
Hirose, N., K. Nishimura, and M. Yamamoto (2009), Observational evidence of a warm ocean current preceding a winter teleconnection pattern in the northwestern Pacific, *Geophys. Res. Lett.*, *36*, L09705, doi:10.1029/2009GL037448.
Inatsu, M., H. Mukougawa, and S. P. Xie (2003), Atmospheric response to zonal variations in midlatitude SST: Transient and stationary eddies and their feedback*, *J. Clim.*, *16*(20), 3314–3329.
Isoda, Y. (1994), Interannual SST variations to the north and south of the polar front in the Japan Sea, *La mer*, *32*(4), 285–293.
Isoda, Y., S. Saitoh, and M. Mihara (1991), SST structure of the polar front in the Japan Sea, *Elsevier Oceanogr. Ser.*, *54*, 103–112, doi:10.1016/S0422-9894(08)70089-8.
Kara, A. B., P. A. Rochford, and H. E. Hurlburt (2003), Mixed layer depth variability over the global ocean, *J. Geophys. Res.*, *108*(C3), 3079, doi:10.1029/2000JC000736.
Kazmin, A. S., and M. M. Rienecker (1996), Variability and frontogenesis in the large-scale oceanic frontal zones, *J. Geophys. Res.*, *101*(C1), 907–921, doi:10.1029/95JC02992.
Levitus, S. (1983), Climatological Atlas of the World Ocean, *Eos Trans. AGU*, *64*(49), 962–963, doi:10.1029/EO064i049p00962-02.
Minobe, S., A. K. Yoshida, N. Komori, S. P. Xie, and R. J. Small (2008), Influence of the Gulf Stream on the troposphere, *Nature*, *452*(7184), 206–209, doi:10.1038/nature06690.
Miyazawa, Y., R. Zhang, X. Guo, H. Tamura, D. Ambe, J. S. Lee, A. Okuno, H. Yoshinari, T. Setou, and K. Komatsu (2009), Water mass variability in the western North Pacific detected in a 15-year eddy resolving ocean reanalysis, *J. Oceanogr.*, *65*(6), 737–756, doi:10.1007/s10872-009-0063-3.
Moisan, J. R., and P. P. Niiler (1998), The seasonal heat budget of the North Pacific: Net heat flux and heat storage rates (1950–1990), *J. Phys. Oceanogr.*, *28*(3), 401–421, doi:10.1175/1520-0485(1998)028<0401:TSHBOT>2.0.CO;2.
Moteki, Q., and A. Manda (2013), Seasonal migration of the Baiu Frontal Zone over the East China Sea: Sea surface temperature effect, *SOLA*, *9*, 19–22, doi:10.2151/sola.2013-005.
Noh, Y., and H. J. Kim (1999), Simulations of temperature and turbulence structure of the oceanic boundary layer with the improved near-surface process, *J. Geophys. Res.*, *104*(C7), 15,621–15,634, doi:10.1029/1999JC900068.
Nonaka, M., H. Nakamura, B. Taguchi, N. Komori, A. K. Yoshida, and K. Takaya (2009), Air-sea heat exchanges characteristic of a prominent midlatitude oceanic front in the South Indian Ocean as simulated in a high-resolution coupled GCM, *J. Clim.*, *22*(24), 6515–6535, doi:10.1175/2009JCLI2960.1.
Ogawa, F., H. Nakamura, K. Nishii, T. Miyasaka, and A. K. Yoshida (2012), Dependence of the climatological axial latitudes of the tropospheric westerlies and storm tracks on the latitude of an extratropical oceanic front, *Geophys. Res. Lett.*, *39*, L05804, doi:10.1029/2011GL049922.
Park, J. H., and D. R. Watts (2005), Response of the southwestern Japan/East Sea to atmospheric pressure, *Deep Sea Res., Part II*, *52*(11), 1671–1683, doi:10.1016/j.dsr2.2003.08.007.
Park, K., D. S. Ullman, K. Kim, J. Y. Chung, and K. R. Kim (2007), Spatial and temporal variability of satellite-observed subpolar front in the East/Japan Sea, *Deep Sea Res., Part I*, *54*(4), 453–470, doi:10.1016/j.dsr.2006.12.010.
Park, K. A., J. Y. Chung, and K. Kim (2004), Sea surface temperature fronts in the East (Japan) Sea and temporal variations, *Geophys. Res. Lett.*, *31*, L07304, doi:10.1029/2004GL019424.
Paulson, C. A., and J. J. Simpson (1977), Irradiance measurements in the upper ocean, *J. Phys. Oceanogr.*, *7*(6), 952–956, doi:10.1175/1520-0485(1977)007<0952:IMITUO>2.0.CO;2.
Qiu, C., and H. Kawamura (2012), Study on SST front disappearance in the subtropical North Pacific using microwave SSTs, *J. Oceanogr.*, *1–10*, doi:10.1007/s10872-012-0106-z.
Reynolds, R. W., N. A. Rayner, T. M. Smith, D. C. Stokes, and W. Wang (2002), An improved in situ and satellite SST analysis for climate, *J. Clim.*, *15*(13), 1609–1625.
Sampe, T., H. Nakamura, A. Goto, and W. Ohfuchi (2010), Significance of a midlatitude SST frontal zone in the formation of a storm track and an eddy-driven westerly jet, *J. Clim.*, *23*(7), 1793–1814, doi:10.1175/2009JCLI3163.1.
Seo, H., M. Jochum, R. Murtugudde, A. J. Miller, and J. O. Roads (2007), Feedback of tropical instability-wave-induced atmospheric variability onto the ocean, *J. Clim.*, *20*(23), 5842–5855, doi:10.1175/JCLI4330.1.
Stevenson, J. W., and P. P. Niiler (1983), Upper ocean heat budget during the Hawaii-to-Tahiti shuttle experiment, *J. Phys. Oceanogr.*, *13*(10), 1894–1907, doi:10.1175/1520-0485(1983)013<1894:UOHBDT>2.0.CO;2.
Takikawa, T., and J. H. Yoon (2005), Volume transport through the Tsushima Straits estimated from sea level difference, *J. Oceanogr.*, *61*(4), 699–708, doi:10.1007/s10872-005-0077-4.
Thomson, R. E., and I. V. Fine (2003), Estimating mixed layer depth from oceanic profile data, *J. Atmos. Oceanic Technol.*, *20*(2), 319–329, doi:10.1175/1520-0426(2003)020<0319:EMLDFO>2.0.CO;2.
Xie, S. P., J. Hafner, Y. Tanimoto, W. T. Liu, H. Tokinaga, and H. Xu (2002), Bathymetric effect on the winter sea surface temperature and climate of the Yellow and East China Seas, *Geophys. Res. Lett.*, *29*(24), 2228, doi:10.1029/2002GL015884.
Yamamoto, M., and N. Hirose (2007), Impact of SST reanalyzed using OGCM on weather simulation: A case of a developing cyclone in the Japan Sea area, *Geophys. Res. Lett.*, *34*, L05808, doi:10.1029/2006GL028386.
You, Y., K. I. Chang, J. Y. Yun, and K. R. Kim (2010), Thermocline circulation and ventilation of the East/Japan Sea, part I: Water-mass characteristics and transports, *Deep Sea Res., Part II*, *57*(13), 1221–1246, doi:10.1016/j.dsr2.2009.12.011.